

ARTICLE

Benchmarking Nitrous Oxide Adsorption and Activation in Metal-Organic Frameworks Bearing Coordinatively Unsaturated Metal Centers

Received 00th January 20xx,
Accepted 00th January 20xx

DOI: 10.1039/x0xx00000x

Tristan A. Pitt,^a Haojun Jia,^{b,c} Tyler J. Azbell,^a Mary E. Zick,^a Aditya Nandy,^{b,c} Heather J. Kulik,^{b,c} Phillip J. Milner^{a,*}

Anthropogenic emissions of N₂O, the third most abundant greenhouse gas after CO₂ and CH₄, are contributing to global climate change. Although metal-organic frameworks (MOFs) have been widely studied as adsorbents for CO₂ and CH₄, less effort has focused on the use of MOFs to remove N₂O from emission streams or from air. Further, N₂O activation would enable its use as an inexpensive oxidant for fine chemical synthesis. Herein, we identify features that contribute to strong binding and high uptake of N₂O at coordinatively unsaturated metal sites in the M₂Cl₂(btdd) (M = Mn, Co, Ni, Cu; btdd²⁻ = bis(1,2,3-triazolo[4,5-b],[4',5'-i])dibenzo[1,4]dioxin) and M₂(dobdc) (M = Mg, Mn, Fe, Co, Ni, Cu, Zn; dobdc⁴⁻ = 2,5-dioxido-1,4-benzenedicarboxylate) series of MOFs. Combined experimental and computational studies suggest that N₂O adsorption at open-metal-sites is primarily based on electrostatic interactions, rather than π -backbonding, causing MOFs with more Lewis acidic metal centers to be superior N₂O adsorbents. As a result, Mg₂(dobdc) demonstrates strong binding and record-setting N₂O uptake (8.75 mmol/g at 1 bar and 298 K). Using density functional theory (DFT) to characterize reactive intermediates and transition states, we demonstrate that N₂O activation to form a M(IV)-oxo species and N₂ is thermodynamically favorable in Mn₂(dobdc) and Fe₂(dobdc) but appears to be kinetically limited in Mn₂(dobdc). Our work lays a foundation for understanding N₂O adsorption and activation in MOFs, paving the way for the design of promising next-generation materials for N₂O capture and utilization.

Introduction

N₂O is the third most prevalent anthropogenic greenhouse gas after CO₂ and CH₄, accounting for 6% of the effective radiative forcing from 1960 to 2019.¹ Although CO₂ and CH₄ are present in higher concentrations in the atmosphere, the global warming potential of N₂O (265) is far greater (1 and 28 for CO₂ and CH₄, respectively) and its atmospheric lifetime (116 y) is far longer (1 and 12 y for CO₂ and CH₄, respectively).² Over the last four decades, global anthropogenic emissions of N₂O have increased by 30%.³ Up to 87% of this increase derives from agricultural practices such as nitrogen additions to soils. By nature, the sources of these emissions (i.e., farmlands) are diffuse, in contrast to point sources of N₂O emissions such as adipic and nitric acid manufacturing.⁴ Diffuse emissions are currently largely uncontrolled, except for preventative measures such as the use of more efficient fertilizers.^{5,6} At point

sources, N₂O can be catalytically destroyed, but regulations requiring this practice have not been globally adopted.⁷ Thus, the majority of human-caused N₂O emissions are currently unabated, leading to a current estimated rate of increase in atmospheric N₂O concentration of 2% per decade.³ In addition to its global warming potential, N₂O was found to be the dominant ozone-depleting substance emitted in the 21st century,⁴ underscoring the urgency of curtailing N₂O emissions. The environmental effects of anthropogenic N₂O emissions and its long atmospheric lifetime necessitate the development of new materials for N₂O capture.

Selectively capturing gases from diffuse sources such as air is a unique challenge that requires specially designed sorbents. Metal-organic frameworks (MOFs) are an emerging class of materials that have drawn significant interest for their potential applications in greenhouse gas capture,⁸ separations,⁹ catalysis,¹⁰ and beyond.¹¹ They are crystalline, highly porous materials formed by connecting metal secondary building units (SBU) with multitopic organic linkers. MOFs have been designed to selectively bind CO₂ and CH₄ based on electrostatic interactions,^{12,13} chemical reactivity,^{14–16} hydrogen bonding,¹⁷

^a Department of Chemistry and Chemical Biology, Cornell University, Ithaca, NY, 14850, United States.

^b Department of Chemical Engineering, Massachusetts Institute of Technology, Cambridge, MA, 02139, United States.

^c Department of Chemistry, Massachusetts Institute of Technology, Cambridge, MA, 02139, United States.

Electronic Supplementary Information (ESI) available: Synthesis, characterization, and gas sorption measurements of all MOFs, additional computational details, and high-temperature N₂O experiments. See DOI: 10.1039/x0xx00000x

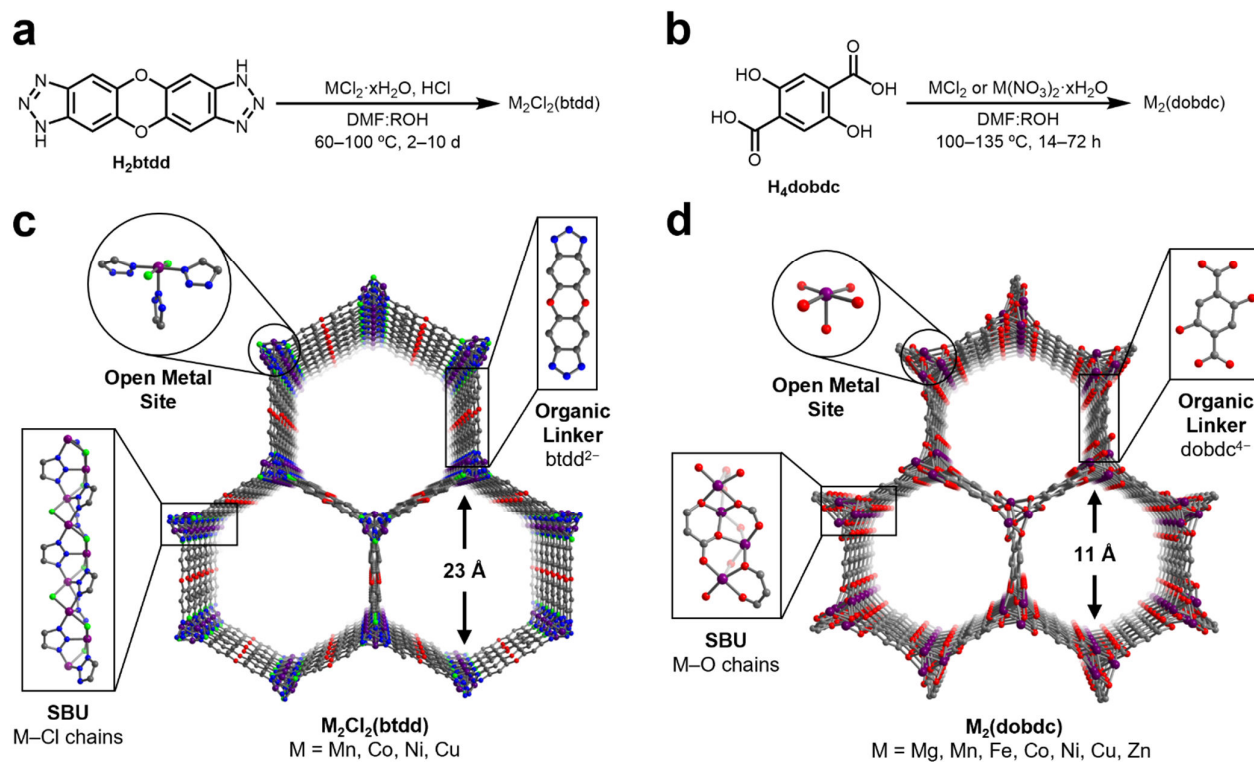


Figure 1. General synthesis conditions of a) $\text{M}_2\text{Cl}_2(\text{btdd})$ (M = Mn, Co, Ni, Cu) and b) $\text{M}_2(\text{dobdc})$ (M = Mg, Mn, Fe, Co, Ni, Cu, Zn) MOFs (R = Et, Me, *i*Pr, H). Structures of c) $\text{M}_2\text{Cl}_2(\text{btdd})$ and d) $\text{M}_2(\text{dobdc})$. Purple, light green, blue, grey, and red spheres represent metal, chlorine, nitrogen, carbon, and oxygen atoms, respectively. Hydrogen atoms are omitted for clarity.

and more. In contrast, only a small number of largely unrelated MOFs have been studied for N_2O capture to date.^{18–25} The presence of Lewis acidic open-metal-sites has been shown to enhance N_2O binding;¹⁹ however, a general lack of structure-property trends informing the design of new materials hinders improvements in N_2O capture in porous materials.

Herein, we present a structure-activity study of N_2O adsorption in MOFs, with the purpose of identifying features that lead to strong binding and high uptake. Through a combined experimental and computational analysis, we clarify the effects of the ligand field and metal identity on N_2O adsorption at Lewis acidic open-metal-sites in the $\text{M}_2\text{Cl}_2(\text{btdd})$ (M = Mn, Co, Ni, Cu; btdd^{2-} = bis(1,2,3-triazolo[4,5-b], [4',5'-i])dibenzo[1,4]dioxin)^{26–28} and $\text{M}_2(\text{dobdc})$ (M = Mg, Mn, Fe, Co, Ni, Cu, Zn; dobdc^{4-} = 2,5-dioxido-1,4-benzenedicarboxylate) series of MOFs.^{12,29,30} From this analysis, we identify the $\text{M}_2(\text{dobdc})$ series, particularly $\text{Mg}_2(\text{dobdc})$ and $\text{Ni}_2(\text{dobdc})$, as promising adsorbents that display strong binding and record-setting N_2O adsorption capacities.

Beyond reducing its environmental impact, N_2O capture is incentivized by the opportunity to utilize it as a cheap, abundant, and potent oxidant in organic synthesis.^{31–33} As a kinetically inert molecule, transition metal catalysts and/or high temperatures and pressures are required to facilitate N_2O activation. Thus, MOFs and zeolites containing Fe(II) sites have been explored as catalysts for N_2O functionalization.^{34–39} In particular, $\text{Fe}_2(\text{dobdc})$ has been demonstrated to catalyze C–H oxidation of hydrocarbons using N_2O as an oxidant.^{37,40–42}

Bearing strong similarities to enzymatic iron-based catalysts,^{43–45} this occurs through a $2e^-$ transfer from high spin Fe(II) to the oxygen of N_2O , cleaving the N–O bond and forming a high spin Fe(IV)–oxo intermediate. This process is calculated to be followed by σ -attack and H atom abstraction by the Fe(IV)–oxo and radical rebound to generate the oxidized product.⁴⁰ Herein, DFT calculations support that N_2O activation is also thermodynamically favorable in $\text{Mn}_2(\text{dobdc})$, and we map out an approximate reaction coordinate for this process using the climbing-image nudged elastic band method (CI-NEB). While combined analysis of computation and experiment suggests that this reaction is kinetically limited in $\text{Mn}_2(\text{dobdc})$, our work motivates further study of N_2O activation in related Mn-based MOFs. Overall, our findings stimulate the development of new framework materials for selective N_2O capture and conversion to mitigate its environmentally destructive impact.

Results and Discussion

N_2O adsorption analysis.

N_2O is a weakly σ -donating and π -accepting ligand, which has limited the number of well-characterized transition metal adducts of N_2O to only a small handful, typically bound as $\eta^1\text{-N}$ or $\eta^2\text{-N,N}$ coordinated N_2O through π -backbonding interactions.^{46–52} Although N_2O has a relatively weak dipole moment (0.161 D),⁵³ sorbents could compensate by incorporating Lewis acidic sites to strengthen electrostatic interactions between N_2O and the sorbent material. MOFs

containing highly Lewis acidic coordinatively unsaturated metal centers are effective adsorbents for a wide variety of gases through strong electrostatic interactions.⁵⁴ To identify robust structure-property trends regarding N₂O binding at open-metal-sites, we targeted isostructural frameworks accommodating a range of metal ions in similar ligand fields. These criteria should effectively yield insights into the interplay of the metal identity and ligand field on the binding strength of N₂O at open-metal-sites in MOFs.

Two groups of MOFs that fulfil these requirements are the M₂Cl₂(btdd) and M₂(dobdc) series. These MOFs are composed of hexagonal-pored structures formed by connecting one-dimensional, rod-like metal SBUs with ditopic organic linkers (Figure 1). Porous channels extend through the materials and, after activation, become lined with a high density of coordinatively unsaturated metal sites confined in square pyramidal geometries. While the overall structures of the M₂Cl₂(btdd) and M₂(dobdc) series are similar, their SBUs lead to distinctive ligation of the metal sites. In M₂Cl₂(btdd), metal ions are coordinated to three individual triazolate groups through one nitrogen atom per triazolate. Each triazolate coordinates to three distinct metal ions, and two chlorides (μ_2) bridge neighboring metals, forming M–Cl chains. For this study, the isostructural Mn, Co, Ni, and Cu MOFs of this series were synthesized according to reported procedures (Figure 1a, SI sections 3–6).^{26,28,55} In the M₂(dobdc) series, the secondary building units are composed of metal-salicylate chains, forming an oxygen-based ligand field. The Mg, Mn, Fe, Co, Ni, Cu, and Zn variants of M₂(dobdc) were synthesized in accordance with the literature (Figure 1b, SI sections 7–13).^{12,30,56–59} All MOFs analyzed in this study were confirmed to be highly crystalline and match the expected structures via powder X-ray diffraction (PXRD). The porosity of all MOFs was confirmed using 77 K N₂ adsorption/desorption measurements. The calculated surface areas are similar to those reported in the literature in every case.

After synthesis, the MOFs were each evaluated as N₂O sorbents by measuring N₂O adsorption and desorption isotherms at 25 °C, 35 °C, and 45 °C (SI sections 3–13). Adsorption data were fit using dual-site Langmuir-Freundlich models (SI Eq S1). These fits were subsequently used to calculate enthalpies of N₂O adsorption ($-\Delta H_{ads}$) in each MOF using the Clausius-Clapeyron equation (SI Eq S2). The resulting $-\Delta H_{ads}$ values as a function of N₂O uptake in both series of MOFs are summarized in Figure 2 and Table 1. Critically, PXRD and surface area measurements confirm the stability of every MOF towards N₂O except for Fe₂(dobdc), which has been previously shown to react irreversibly with this gas.^{37,40–42} As a result, the adsorption data for this MOF were excluded from the analysis below.

The M₂Cl₂(btdd) series were first evaluated as N₂O sorbents. Despite their high density of open-metal-sites, all MOFs of this series only weakly interact with N₂O ($-\Delta H_{ads} < 25$ kJ/mol). The difference in binding strength between the variants is minor: Co, Ni, and Mn analogues exhibit similar binding strengths, followed by Cu (Table 1). MOFs bearing coordinatively

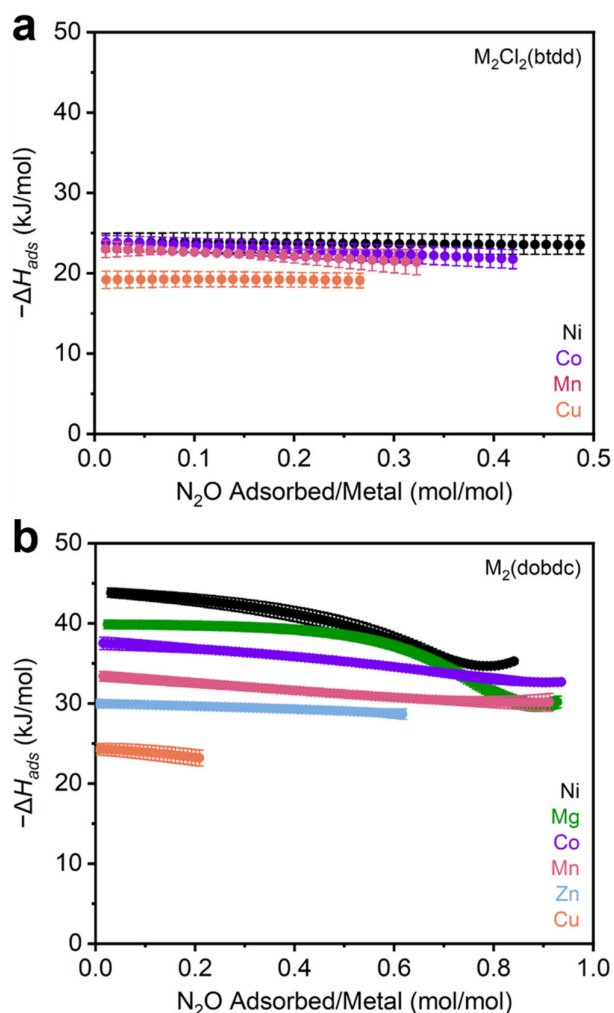


Figure 1. a) $-\Delta H_{ads}$ vs. N₂O uptake calculated from N₂O adsorption isotherms in a) M₂Cl₂(btdd) (M = Ni, Co, Cu, Mn) and b) M₂(dobdc) (M = Ni, Mg, Co, Mn, Zn, Cu) MOFs.

unsaturated Cu sites are commonly poor adsorbents due to Jahn-Teller axial distortion at the Cu sites.^{12,60} Lacking substantial differences in binding strength between variants, the influence of the metal identity appears to be overshadowed by that of the ligand field in the M₂Cl₂(btdd) series. The Lewis acidities of the metals are likely tempered by the electron-donating coordination environment of triazolate and chloride

Table 1 N₂O adsorption enthalpies and maximum uptake values at 298 K in M₂Cl₂(btdd) and M₂(dobdc) MOFs.

MOF	$-\Delta H_{ads}$ N ₂ O (kJ/mol)	Maximum Uptake at 298 K (mmol/g)
Mn ₂ Cl ₂ (btdd)	23.0 ± 1.1	2.37
Co ₂ Cl ₂ (btdd)	23.9 ± 0.8	3.10
Ni ₂ Cl ₂ (btdd)	23.8 ± 1.1	3.49
Cu ₂ Cl ₂ (btdd)	19.2 ± 1.1	1.86
Mg ₂ (dobdc)	39.9 ± 0.5	8.75
Mn ₂ (dobdc)	33.4 ± 0.6	7.77
Co ₂ (dobdc)	37.5 ± 0.8	7.26
Ni ₂ (dobdc)	43.8 ± 0.6	6.44
Cu ₂ (dobdc)	24.3 ± 0.7	2.21
Zn ₂ (dobdc)	30.0 ± 0.5	5.37

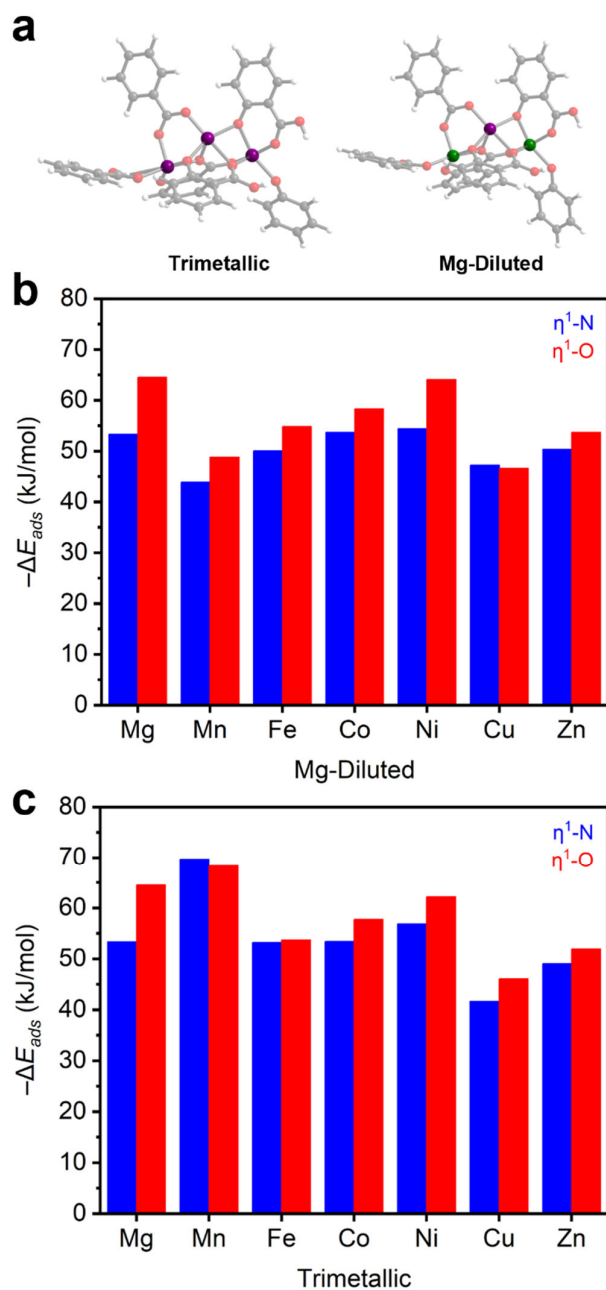


Figure 3. a) Trimetallic (left) and Mg-diluted (right) cluster models of $M_2(dobdc)$. Purple, green, grey, red, and white spheres represent metal, magnesium, carbon, oxygen, and hydrogen atoms, respectively. DFT-calculated negative adsorption energies ($-\Delta E_{ads}$) of η^1 -N (blue) and η^1 -O (red) coordinated N_2O in the b) Mg-diluted and c) trimetallic systems.

ligands. These ligands produce electron-rich metal centers that are less Lewis acidic than those found in other materials. Although these MOFs are capable of binding polar gases such as NH_3 ,²⁶ the absence of a significant dipole moment on N_2O makes the $M_2Cl_2(btdd)$ MOFs ineffective N_2O adsorbents. Lacking suitable binding sites, the $M_2Cl_2(btdd)$ series show very limited uptakes; the quantity of N_2O adsorbed under equilibrium conditions, even at 1000 mbar N_2O and 298 K (Table 1), does not come close to saturating the available open-metal-

Decreasing the ligand field strength surrounding the open-metal-sites should produce more Lewis acidic metal centers and thus lead to stronger electrostatic interactions with N_2O . Switching from $M_2Cl_2(btdd)$ to $M_2(dobdc)$ preserves the coordination geometry of the metal centers, but the oxygen-based SBU provides a weaker ligand field overall. Indeed, every member of the $M_2(dobdc)$ series binds N_2O more strongly at low pressures than the $M_2Cl_2(btdd)$ MOFs (Figure 2b). Moreover, the comparatively electron-deficient coordination environments in this series emphasize the influence of the metal identity on N_2O binding strengths; enthalpies of adsorption vary by as much as 20 kJ/mol among $M_2(dobdc)$ variants (Table 1). N_2O binding strengths in these series mirror the empirical Irving-Williams series: $Cu < Zn < Mn < Co < Mg < Ni$.⁶¹ Like $Cu_2Cl_2(btdd)$, $Cu_2(dobdc)$ likely exhibits weak N_2O adsorption because of axial distortion.¹² In contrast, $Mg_2(dobdc)$ is an especially effective N_2O adsorbent due to the hard nature of its Lewis acidic Mg(II) cations. As the effective charge of the transition metal centers increases from Mn to Ni,⁶² the N_2O binding strengths increase as well. As a result, $Ni_2(dobdc)$ is the strongest N_2O adsorbent assessed in this study ($-\Delta H_{ads} = 43.8 \pm 0.6$ kJ/mol). Compared to other commonly studied gases (CO_2 , O_2 , N_2), N_2O is generally more strongly bound by the $M_2(dobdc)$ series, which is likely due to its modest dipole moment. In particular, N_2O binding is approximately 2–6 kJ/mol stronger than CO_2 in all cases except for in $Mg_2(dobdc)$, in which CO_2 binds more strongly by approximately 3 kJ/mol.¹² O_2 and N_2 binding enthalpies are consistently 10–20 kJ lower than those of N_2O as well.⁶³ These findings highlight the discrepancy between the comparatively strong binding of N_2O at metal centers compared to CO_2 , O_2 , and N_2 and the lack of well-characterized N_2O -bound metal complexes.^{46–50}

Strong N_2O binding is accompanied by relatively high N_2O capacities in the $M_2(dobdc)$ series of frameworks. In particular, the second-strongest adsorbent of N_2O identified in this work, $Mg_2(dobdc)$, adsorbs 8.75 mmol/g at 1000 mbar of N_2O and 298 K, surpassing the previous record-holder, MIL-100 (Cr) (5.78 mmol/g, MIL = Materials Institute Lavoisier), by a significant margin.²⁰ The Mn, Co, and Ni $M_2(dobdc)$ variants also exceed the previous record for N_2O uptake in a MOF. Overall, this comparison underlines the $M_2(dobdc)$ series, especially $Mg_2(dobdc)$, as promising adsorbents that exhibit high gravimetric N_2O capacities coupled with strong and tuneable binding strengths.

Computational survey of N_2O adsorption.

After establishing the $M_2(dobdc)$ series as effective N_2O adsorbents, we further evaluated N_2O binding in this series using DFT calculations (SI section 14). For these calculations, trimetallic cluster models were generated to approximately study the one-dimensional chain SBU (Figure 3a). Similar cluster models have been used to evaluate N_2O reduction in $Fe_2(dobdc)$.^{40,41} For each member of the $M_2(dobdc)$ series, excluding $Mg_2(dobdc)$ for redundancy, two types of cluster models were simulated: a trimetallic system and a Mg-diluted system. In the Mg-diluted models, both edge metal ions were replaced with Mg(II) ions. The purpose of including the Mg-

diluted systems is to simulate only one open-shell metal center and decouple adsorption energetics from the potential influence of metal-metal coupling on N₂O adsorption. All systems are neutral with all M(II) ions in the high-spin state where applicable (SI Table S13).

The energies of adsorption ($-\Delta E_{ads}$) for both η^1 -N and η^1 -O coordinated N₂O adducts in the model clusters were first calculated (Figure 3b–c, SI Table S11). In both the trimetallic and Mg-diluted models, η^1 -O coordinated N₂O is slightly more stabilized (2–10 kJ/mol) than η^1 -N coordinated N₂O. This aligns with the approximately 60%/40% η^1 -O/ η^1 -N population split determined from neutron diffraction data collected on N₂O-dosed Fe₂(dobdc).³⁷ The calculated formation energies of N₂O adducts in the Mg-diluted series (Figure 3b) approximately match the trend observed experimentally: Cu \approx Mn < Fe \approx Zn < Co < Ni \approx Mg. However, some divergence is noted in the trimetallic systems (Figure 3c): the Mn-based trimetallic system binds N₂O considerably more strongly than the equivalent Mg-diluted model, suggesting multiple metal effects that require consideration of metal-metal coupling (see below). Additionally, η^1 -N coordination to Mn₂(dobdc) is slightly more favorable than η^1 -O in the trimetallic model.

Across the series, the model systems reveal that η^1 -O and η^1 -N adducts of N₂O are bent, with bond angles and M–N₂O distances in agreement with those solved from the neutron diffraction data in N₂O–Fe₂(dobdc) (SI Table S12), the only definitively characterized structure of N₂O bound to a metal center within a MOF reported to date.³⁷ In the DFT-calculated structure, η^1 -N coordinated N₂O exhibits a typical bond angle of 115–123° (122° in N₂O–Fe₂(dobdc)), whereas η^1 -O coordinated N₂O exhibits slightly smaller bond angles ranging from 105–120° (117° in N₂O–Fe₂(dobdc)). Bond lengths of η^1 -N and η^1 -O coordinated N₂O (2.25–2.57 Å and 2.27–2.54 Å, respectively) vary over only a narrow range. These models reinforce that N₂O binding across the M₂(dobdc) series is primarily based on electrostatic interactions rather than π -backbonding, which would be expected to lead to linear η^1 -N (V, Cu, Ru, Rh) or side-on η^2 -N,N (Co, Ni) interactions with N₂O.^{46–52}

It should be noted that N₂O adsorption has been modelled previously in a small variety of other open-metal-site MOFs. The Fe(II)- and Cu(II)-based paddlewheel nodes in M₃(btc)₂ (btc³⁻ = benzene-1,3,5-tricarboxylate) MOFs show bent η^1 -N and η^1 -O coordination modes for N₂O.⁵⁴ Likewise, N₂O adducts have been modelled for the trinuclear carboxylate-bridged, oxygen-centered nodes (M₃(μ_3 -O)(RCOO)₆, M = V, Cr, Mn, Fe, Co, Ni) common among MOFs such as MIL-100, MIL-101, and MIL-127.⁶⁴ The calculated binding of η^1 -N coordinated N₂O at V centers is linear, but other adducts are bent, with similar bond angles and bond lengths as calculated in the M₂(dobdc) series herein. In the Kuratowski-type SBU of Cu-MFU-4l (MFU = Metal-Organic Framework Ulm-University), DFT calculations support an approximately linear η^1 -N coordinated N₂O molecule, indicating possible π -backbonding from the Cu(I) centers.¹⁹ Overall, these findings support that N₂O is predicted to bind in a bent fashion at most metal centers in MOFs.

A notable exception to the trends outlined above is the trimetallic Mn cluster, in which η^1 -N coordinated N₂O is nearly

linear (172°), suggesting that π -backbonding occurs from the Mn *d* orbitals into the π^* orbital of N₂O, which has previously been invoked in linear η^1 -N V, Cu, Ru, and Rh adducts of N₂O to justify the stability of those complexes.^{46,48–50,52} Consistently, the Mn–N bond length (1.95 Å) is considerably shorter than in other models (SI Figure S68). These characteristics are distinct from the equivalent Mg-diluted cluster, suggesting that metal-metal coupling may affect the binding mode of N₂O in these calculations. We thus evaluated N₂O binding in the open-shell trimetallic systems (Mn through Cu) using broken-symmetry density functional theory (BS-DFT) with two spin flip configurations (i.e., in the central metal or in one edge metal) to quantify the metal-metal coupling and to extract coupling constants (SI Figure S69, SI section 14). To ensure that the BS-DFT calculations converged to the desired states, the spin density was visually inspected (SI Figure S70). In particular, the energetic difference in the trimetallic Mn system in comparison to the dilute case indicates especially strong metal-metal coupling (SI Table S14). From this data, we calculated strong magnetic coupling along the SBU chains in the trimetallic Mn system ($J = 314.27 \text{ cm}^{-1}$), which becomes even stronger after N₂O binding regardless of the coordination mode ($J = 857.47 \text{ cm}^{-1}$ for η^1 -N, $J = 857.47 \text{ cm}^{-1}$ for η^1 -O). Consistently, magnetic susceptibility measurements (SI Figure S77) and prior first principles studies support that Mn₂(dobdc) exhibits antiferromagnetic coupling below approximately 27 K.^{62,65} Adsorbate-induced changes in magnetic coupling are also preceded in the M₂(dobdc) series; for example, in Fe₂(dobdc), the ferromagnetic exchange strength along the SBU chains is attenuated by interaction with weak adsorbates (e.g., CH₄, $-\Delta H_{ads} = 20 \text{ kJ/mol}$), and the coupling becomes antiferromagnetic upon interaction with strong adsorbates (e.g., C₂H₂, $-\Delta H_{ads} = 47 \text{ kJ/mol}$).⁶⁶ Our results point to an additional stabilization of the N₂O adducts of Mn₂(dobdc) related to enhanced metal coupling, possibly leading to greater π -backbonding from Mn to N₂O and favoring linear η^1 -N coordination. Above 27 K, however, this effect is no longer expected to significantly contribute to the adsorption interactions as the spins become randomly oriented. Consistently, the experimental binding enthalpies do not show enhanced adsorption in Mn₂(dobdc) relative to other MOFs in the series. Nevertheless, if a suitable Mn-based open-metal-site MOF with a higher Neel temperature were to be identified, this feature could potentially be leveraged to enhance N₂O binding.

Evaluating N₂O activation in the M₂(dobdc) series.

N₂O activation to form M(IV)-oxo species and N₂ in MOFs has been principally studied in Fe₂(dobdc) and other Fe(II)-based frameworks.^{37–41,67,68} Unfortunately, Fe(II)-based systems are prohibitively air sensitive for practical applications. Identifying more air-stable materials capable of N₂O activation would be a significant step towards utilizing N₂O as a green oxidant. In order to determine whether this reactivity is unique to Fe₂(dobdc), the same cluster models were used to calculate the favorability of M(IV)-oxo formation in the remainder of the M₂(dobdc) series (SI Table S15, SI section 14). DFT calculations with both the trimetallic and Mg-diluted cluster model series

show that, in addition to $\text{Fe}_2(\text{dobdc})$, M(IV)-oxo formation is thermodynamically favorable ($\Delta E_f < 0$ kJ/mol) in $\text{Mn}_2(\text{dobdc})$ (Figure 4a, SI section 14). Indeed, M(IV)-oxo formation is calculated to be significantly more thermodynamically favorable in $\text{Mn}_2(\text{dobdc})$ (−183.1 and −176.1 kJ/mol for trimetallic and Mg-diluted systems, respectively) than in $\text{Fe}_2(\text{dobdc})$ (−55.5 and −52.7 kJ/mol for trimetallic and Mg-diluted systems, respectively). In contrast, M(IV)-oxo formation is endothermic in the Mg, Co, Ni, Cu, and Zn analogues, ruling out these materials as potential catalysts for N_2O activation. This is fairly expected due to the electronic instability of terminal M(IV)-oxo complexes of octahedral symmetry possessing greater than 5 *d* electrons.⁶⁹ Precedent for N_2O activation in Mn-based systems is found in manganese oxides, which catalyze the decomposition of N_2O ⁷⁰ and the oxidation of 1-butene at high temperatures.⁷¹ Likewise, Mn-substituted polyoxometalates have been shown to activate N_2O and catalyze the epoxidation of alkenes,^{72,73} and Mn-substituted zeolites catalyze N_2O decomposition as well.^{74,75}

To determine the potential viability of N_2O activation by $\text{Mn}_2(\text{dobdc})$, an approximate reaction coordinate for this process was modelled using the CI-NEB method (Figure 4b, Text S1). The $\eta^1\text{-O}$ coordinated N_2O adduct of the Mg-diluted $\text{Mn}_2(\text{dobdc})$ cluster model was used as the initial state, and the Mn(IV)-oxo-containing Mg-diluted cluster was used as the final state (SI section 14). During N_2O activation, the Mn(IV)-oxo bond is formed and the O–N bond is broken, forming N_2 . From the initial state, the M–O bond length shrinks significantly and is matched by a substantial lengthening of the O–N bond. During this transition, the energy of the system rises sharply early on, after which it falls to roughly the energy of the final state. Likewise, a constant M–O bond length, consistent with Mn(IV)-oxo formation, was observed in the second half of the reaction coordinate, as the rest of the pathway is characterized by O–N bond elongation as unbound N_2 moves away from the cluster. The approximate transition state of the reaction is rather early, with Mn–O and N–O bond lengths of 2.00 Å and 1.39 Å, respectively (Figure 4c). From the difference in energy between the initial state and this approximate transition state, the kinetic barrier to N_2O activation in this model cluster was calculated to be approximately 113 kJ/mol. This barrier is comparable to the calculated activation barriers of 167 kJ/mol in the Mn-based trinuclear MOF nodes and 109 kJ/mol in the Mn-substituted polyoxometalate discussed above.^{64,73}

In previous studies, heating N_2O -dosed $\text{Fe}_2(\text{dobdc})$ at only 35 °C was sufficient to partially oxidize the material, and its complete oxidation was accomplished at 60 °C after prolonged heating.³⁷ The activation barrier for Fe(IV)-oxo formation in N_2O -bound $\text{Fe}_2(\text{dobdc})$ was calculated to be 94 kJ/mol (enthalpy of activation = 82 kJ/mol).⁴⁰ While we note that the method used to calculate the barrier in $\text{Fe}_2(\text{dobdc})$ differs from this work, it is nonetheless a useful comparison. Although the calculated activation barrier for Mn(IV)-oxo formation in $\text{Mn}_2(\text{dobdc})$ is notably larger, the conditions that lead to Fe(IV)-oxo formation in $\text{Fe}_2(\text{dobdc})$ are mild. As such, we evaluated whether more forceful conditions (i.e., higher temperatures) could enable Mn(IV)-oxo formation in $\text{Mn}_2(\text{dobdc})$. To probe

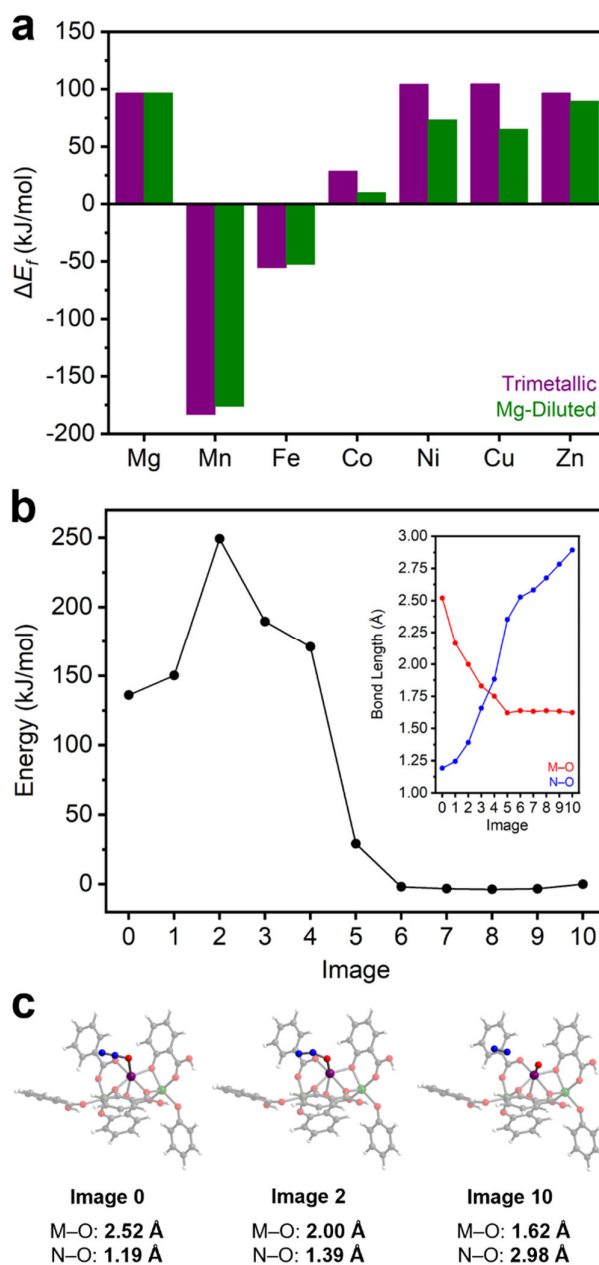


Figure 4. a) DFT-calculated energies of M-oxo formation (ΔE_f) in the trimetallic (purple) and Mg-diluted (green) models of $\text{Mn}_2(\text{dobdc})$. b) CI-NEB-calculated approximate reaction coordinate of Mn-oxo formation from $\eta^1\text{-O}$ coordinated N_2O in the Mg-diluted system. Inset: M–O (red) and N–O (blue) bond lengths vs. image number. c) Structures of the initial (left), transition (center), and final (right) states. Purple, green, blue, grey, red, and white spheres represent manganese, magnesium, nitrogen, carbon, oxygen, and hydrogen atoms, respectively.

this possibility, N_2O adsorption measurements in $\text{Mn}_2(\text{dobdc})$ at 180 °C, 250 °C, and 300 °C were collected to identify potential N_2O activation through changes in the adsorption properties of the material (SI Figure S72). Fully reversible N_2O adsorption was measured at 180 °C; however, measurements at 250 °C and 300 °C consistently yielded anomalous negative adsorption, possibly indicating reactivity with the MOF. For further analysis, a bulk sample of $\text{Mn}_2(\text{dobdc})$ was prepared by dosing the MOF with N_2O at 300 °C (SI section 15). The BET surface area of $\text{Mn}_2(\text{dobdc})$ after heating at 300 °C (1285 ± 3 m²/g) under

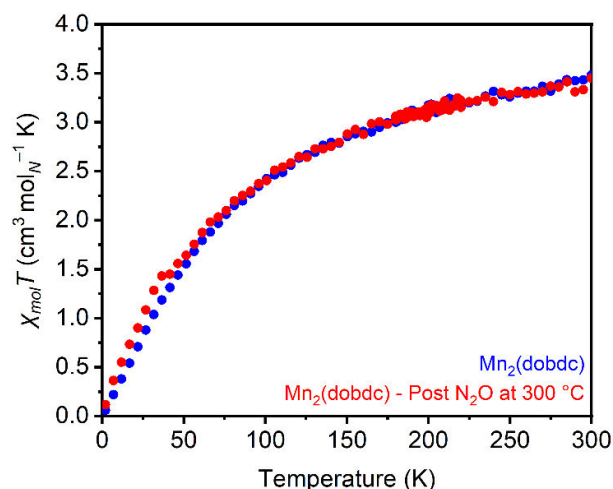


Figure 5. Variable-temperature magnetic susceptibility ($\chi_{mol}T$) measurements of $Mn_2(dobdc)$ under an applied field of 1000 Oe before (blue) and after (red) N_2O treatment at 300 °C. The minor increase in $\chi_{mol}T$ of the N_2O -treated sample from approximately 2–40 K is attributed to slight O_2 contamination.

vacuum for 24 h is comparable to that of the pristine MOF ($1344 \pm 3 \text{ m}^2/\text{g}$), supporting that this MOF is stable at elevated temperatures. Notably, the BET surface area is significantly attenuated after N_2O dosing at 300 °C ($896 \pm 2 \text{ m}^2/\text{g}$) (SI Figure S73). The reduction in surface area is accompanied by a color change from orange to brown. PXRD measurements confirm that $Mn_2(dobdc)$ retains its crystallinity after this process, although some peak-broadening was observed, indicative of partial decomposition (SI Figure S74).

Magnetic susceptibility measurements were used to characterize the product(s) resulting from high-temperature treatment of $Mn_2(dobdc)$ with N_2O . The magnetic moments in $Mn_2(dobdc)$ calculated from susceptibility measurements before ($\mu_{eff} = 5.94 \mu_B$) and after ($\mu_{eff} = 5.89 \mu_B$) (Figures S80–81) N_2O treatment at 300 °C closely match the value expected for Mn(II) with a spin of 5/2 ($5.92 \mu_B$), indicating a lack of oxidation at the metal center after N_2O treatment (Figure 5). Despite this, increased magnetic susceptibility relative to unreacted $Mn_2(dobdc)$ was consistently noted in moment vs. field measurements collected at 5 K after N_2O treatment at 300 °C (SI Figure S82). This finding may point to reactivity between N_2O and the redox-active linker instead,⁷⁶ as oxidation of the high-spin Mn(II) sites to Mn(IV) should result in a decrease in the magnetic susceptibility.

To further characterize the reaction of $Mn_2(dobdc)$ with N_2O , we utilized variable-temperature diffuse reflectance Fourier transform (DRIFTS) spectroscopy (SI Figures S75–76). A sample of $Mn_2(dobdc)$ was heated under an atmosphere of N_2O (approx. 1 bar) from 25 °C to 300 °C and held at 300 °C for 15 h. Spectra were collected periodically throughout the duration of the measurement. New Mn–O stretches corresponding to Mn(IV)–oxo (approx. 845 cm^{-1})⁷⁷ or Mn(III)–OH species ($600\text{--}700 \text{ cm}^{-1}$)⁷⁸ were not observed (SI Figure S76). Likewise, stretches corresponding to quinone formation due to linker oxidation were not observed (1657 cm^{-1}).⁷⁶ However, a weak O–H stretching frequency at 3673 cm^{-1} emerged over time, and the prominent stretch at 1406 cm^{-1} reduced in intensity after prolonged treatment with N_2O (SI Figure S75). Overall, while the

MOF appears to react with N_2O at high temperatures, the DRIFTS and magnetic data indicate a lack of oxidation at the metal centers. This finding suggests that the high kinetic barrier to Mn(IV)–oxo formation in $Mn_2(dobdc)$ is likely prohibitive, despite its thermodynamic favorability. Elucidating the products of this MOF's reaction with N_2O is the focus of ongoing work.

Conclusions

Herein, we identify features that contribute to strong binding and high uptake of N_2O at Lewis acidic, coordinatively unsaturated metal sites in MOFs. We utilize the $M_2Cl_2(btdd)$ and $M_2(dobdc)$ series as model systems to facilitate comparisons, as their general structures are related but distinguished by the ligation of the open-metal-sites. In the $M_2Cl_2(btdd)$ series, the binding enthalpies of N_2O are generally low (<25 kJ/mol) and within error, despite variations in the metal identity. In contrast, the salicylate-based SBU in the $M_2(dobdc)$ series provides a weaker, oxygen-based ligand field. N_2O binding strengths in these MOFs mostly mirror the Irving-Williams series, with $Ni_2(dobdc)$ exhibiting the strongest adsorption of N_2O among all tested MOFs ($-\Delta H_{ads} = 43.8 \pm 0.6$). Notably, $Mg_2(dobdc)$ exhibits a record-breaking N_2O gravimetric capacity (8.75 mmol/g at 1000 mbar of N_2O and 298 K) among MOFs. While these Lewis acidic sites are effective for N_2O capture, they are not necessarily selective for N_2O among other polar(izable) gases, such as H_2O .⁷⁹ Achieving selective adsorption of N_2O at open-metal-sites will be the focus of future work.

Using the cluster systems to computationally model the oxidation of the $M_2(dobdc)$ series by N_2O , forming M(IV)–oxo species, we find that M–oxo formation is also thermodynamically favorable in $Mn_2(dobdc)$ according to DFT calculations. We thus used the CI-NEB method to map a reaction coordinate for this process and determined an approximate activation barrier of 113 kJ/mol, which is higher than that calculated for $Fe_2(dobdc)$ (94 kJ/mol). Although experiments indicate that this kinetic barrier is too high to be overcome in $Mn_2(dobdc)$, these findings suggest that Mn-based MOFs may be promising alternatives to traditionally studied Fe-based materials for N_2O activation.

Overall, this work adds to the growing body of research seeking to utilize N_2O as a green oxidant, in which Mn-based solid-state catalysts remain relatively understudied. The results reported herein will help to drive the identification and development of other effective MOF-based sorbents to mitigate environmentally destructive N_2O emissions.

Author Contributions

P.J.M and H.J.K. conceived the project. T.A.P. carried out the synthesis, characterization, and gas sorption measurements of MOF samples under the supervision of P.J.M. P.J.M. and M.E.Z. also synthesized MOF samples. H.J. and A.N. carried out computational studies under the supervision of H.J.K. T.J.A. carried out magnetic

measurements. T.A.P. and H.J. prepared the first draft of the manuscript, which was edited and approved by all co-authors.

Conflicts of Interest

P.J.M. is listed as a co-inventor on several patents related to metal-organic frameworks.

Acknowledgements

This work was supported by the U.S. Department of Energy, Office of Science, Office of Basic Energy Sciences under Award Number DE-SC0021000 (T.A.P., T.J.A., M.E.Z., P.J.M.). Computational modeling was supported by the National Science Foundation under Award Number CBET-1846426 (H.J., A.N., H.J.K.) as well as a National Science Foundation Graduate Research Fellowship under Grant #1122374 (to A.N.). T.J.A. thanks Cornell University for financial support through a recruiting fellowship. We acknowledge the support of a Camille Dreyfus Teacher-Scholar Award to P.J.M. (TC-23-048). This work made use of a Bruker 500 MHz spectrometer, the purchase of which was supported by the National Science Foundation (CHE-1531632). This work made use of the Cornell Center for Materials Research Shared Facilities, which are supported through the NSF MRSEC program (DMR-1719875). This work was carried out in part using computational resources from the Extreme Science and Engineering Discovery Environment (XSEDE), which is supported by National Science Foundation grant number ACI-1548562. We thank Prof. Joseph Zadrozny (the Ohio State University) for helpful discussions.

Notes and References

- Davidson, E. A.; Winiwarter, W. Urgent Abatement of Industrial Sources of Nitrous Oxide. *Nat. Clim. Chang.* **2023**, *13* (7), 599–601. <https://doi.org/10.1038/s41558-023-01723-3>.
- Intergovernmental Panel On Climate Change. *Climate Change 2021 – The Physical Science Basis: Working Group I Contribution to the Sixth Assessment Report of the Intergovernmental Panel on Climate Change*, 1st ed.; Cambridge University Press, 2023. <https://doi.org/10.1017/9781009157896>.
- Tian, H.; Xu, R.; Canadell, J. G.; Thompson, R. L.; Winiwarter, W.; Suntharalingam, P.; Davidson, E. A.; Ciais, P.; Jackson, R. B.; Janssens-Maenhout, G.; Prather, M. J.; Regnier, P.; Pan, N.; Pan, S.; Peters, G. P.; Shi, H.; Tubiello, F. N.; Zaehle, S.; Zhou, F.; Arneeth, A.; Battaglia, G.; Berthet, S.; Bopp, L.; Bouwman, A. F.; Buitenhuis, E. T.; Chang, J.; Chipperfield, M. P.; Dangal, S. R. S.; Dlugokencky, E.; Elkins, J. W.; Eyre, B. D.; Fu, B.; Hall, B.; Ito, A.; Joos, F.; Krummel, P. B.; Landolfi, A.; Laruelle, G. G.; Lauerwald, R.; Li, W.; Lienert, S.; Maavara, T.; MacLeod, M.; Millet, D. B.; Olin, S.; Patra, P. K.; Prinn, R. G.; Raymond, P. A.; Ruiz, D. J.; Van Der Werf, G. R.; Vuichard, N.; Wang, J.; Weiss, R. F.; Wells, K. C.; Wilson, C.; Yang, J.; Yao, Y. A Comprehensive Quantification of Global Nitrous Oxide Sources and Sinks. *Nature* **2020**, *586* (7828), 248–256. <https://doi.org/10.1038/s41586-020-2780-0>.
- Ravishankara, A. R.; Daniel, J. S.; Portmann, R. W. Nitrous Oxide (N₂O): The Dominant Ozone-Depleting Substance Emitted in the 21st Century. *Science* **2009**, *326* (5949), 123–125. <https://doi.org/10.1126/science.1176985>.
- Hassan, M. U.; Aamer, M.; Mahmood, A.; Awan, M. I.; Barbanti, L.; Seleiman, M. F.; Bakhsh, G.; Alkharabsheh, H. M.; Babur, E.; Shao, J.; Rasheed, A.; Huang, G. Management Strategies to Mitigate N₂O Emissions in Agriculture. *Life* **2022**, *12* (3), 439. <https://doi.org/10.3390/life12030439>.
- Gu, B.; Zhang, X.; Lam, S. K.; Yu, Y.; Van Grinsven, H. J. M.; Zhang, S.; Wang, X.; Bodirsky, B. L.; Wang, S.; Duan, J.; Ren, C.; Bouwman, L.; De Vries, W.; Xu, J.; Sutton, M. A.; Chen, D. Cost-Effective Mitigation of Nitrogen Pollution from Global Croplands. *Nature* **2023**, *613* (7942), 77–84. <https://doi.org/10.1038/s41586-022-05481-8>.
- Li, L.; Xu, J.; Hu, J.; Han, J. Reducing Nitrous Oxide Emissions to Mitigate Climate Change and Protect the Ozone Layer. *Environ. Sci. Technol.* **2014**, *48* (9), 5290–5297. <https://doi.org/10.1021/es404728s>.
- Ding, M.; Flaig, R. W.; Jiang, H.-L.; Yaghi, O. M. Carbon Capture and Conversion Using Metal–Organic Frameworks and MOF-Based Materials. *Chem. Soc. Rev.* **2019**, *48* (10), 2783–2828. <https://doi.org/10.1039/C8CS00829A>.
- Firooz, S. K.; Armstrong, D. W. Metal-Organic Frameworks in Separations: A Review. *Analytica Chimica Acta* **2022**, *1234*, 340208. <https://doi.org/10.1016/j.aca.2022.340208>.
- Bavkina, A.; Kolobov, N.; Khan, I. S.; Bau, J. A.; Ramirez, A.; Gascon, J. Metal–Organic Frameworks in Heterogeneous Catalysis: Recent Progress, New Trends, and Future Perspectives. *Chem. Rev.* **2020**, *120* (16), 8468–8535. <https://doi.org/10.1021/acs.chemrev.9b00685>.
- Furukawa, H.; Cordova, K. E.; O’Keeffe, M.; Yaghi, O. M. The Chemistry and Applications of Metal-Organic Frameworks. *Science* **2013**, *341* (6149), 1230444. <https://doi.org/10.1126/science.1230444>.
- Queen, W. L.; Hudson, M. R.; Bloch, E. D.; Mason, J. A.; Gonzalez, M. I.; Lee, J. S.; Gygi, D.; Howe, J. D.; Lee, K.; Darwish, T. A.; James, M.; Peterson, V. K.; Teat, S. J.; Smit, B.; Neaton, J. B.; Long, J. R.; Brown, C. M. Comprehensive Study of Carbon Dioxide Adsorption in the Metal–Organic Frameworks M₂(dobdc) (M = Mg, Mn, Fe, Co, Ni, Cu, Zn). *Chem. Sci.* **2014**, *5* (12), 4569–4581. <https://doi.org/10.1039/C4SC02064B>.
- He, Y.; Zhou, W.; Qian, G.; Chen, B. Methane Storage in Metal–Organic Frameworks. *Chem. Soc. Rev.* **2014**, *43* (16), 5657–5678. <https://doi.org/10.1039/C4CS00032C>.
- Lin, Y.; Kong, C.; Chen, L. Amine-Functionalized Metal–Organic Frameworks: Structure, Synthesis and Applications. *RSC Adv.* **2016**, *6* (39), 32598–32614. <https://doi.org/10.1039/C6RA01536K>.
- Sharifzadeh, Z.; Morsali, A. Amine-Functionalized Metal–Organic Frameworks: From Synthetic Design to Scrutiny in Application. *Coord. Chem. Rev.* **2022**, *459*, 214445. <https://doi.org/10.1016/j.ccr.2022.214445>.
- Zick, M. E.; Cho, D.; Ling, J.; Milner, P. J. Carbon Capture Beyond Amines: CO₂ Sorption at Nucleophilic Oxygen Sites in Materials. *ChemNanoMat* **2023**, *9* (1), e202200436. <https://doi.org/10.1002/cnma.202200436>.
- Li, J.; Han, X.; Zhang, X.; Sheveleva, A. M.; Cheng, Y.; Tuna, F.; McInnes, E. J. L.; McCormick McPherson, L. J.; Teat, S. J.; Daemen, L. L.; Ramirez-Cuesta, A. J.; Schröder, M.; Yang, S. Capture of Nitrogen Dioxide and Conversion to Nitric Acid in a Porous Metal–Organic Framework. *Nat. Chem.* **2019**, *11* (12), 1085–1090. <https://doi.org/10.1038/s41557-019-0356-0>.
- Zhang, X.; Chen, W.; Shi, W.; Cheng, P. Highly Selective Sorption of CO₂ and N₂O and Strong Gas-Framework Interactions in a Nickel(II) Organic Material. *J. Mater. Chem. A* **2016**, *4* (41), 16198–16204. <https://doi.org/10.1039/C6TA06572D>.
- Denysenko, D.; Jelic, J.; Magdysyuk, O. V.; Reuter, K.; Volkmer, D. Elucidating Lewis Acidity of Metal Sites in MFU-4l Metal–Organic Frameworks: N₂O and CO₂ Adsorption in MFU-4l, CuI-

- MFU-4l and Li-MFU-4l. *Microporous and Mesoporous Materials* **2015**, *216*, 146–150. <https://doi.org/10.1016/j.micromeso.2015.03.014>.
- 20 Yang, J.; Du, B.; Liu, J.; Krishna, R.; Zhang, F.; Zhou, W.; Wang, Y.; Li, J.; Chen, B. MIL-100Cr with Open Cr Sites for a Record N₂O Capture. *Chem. Commun.* **2018**, *54* (100), 14061–14064. <https://doi.org/10.1039/C8CC07679K>.
- 21 Ma, L.; Zhang, F.; Li, K.; Zhang, Y.; Song, Z.; Wang, L.; Yang, J.; Li, J. Improved N₂O Capture Performance of Chromium Terephthalate MIL-101 via Substituent Engineering. *J. Solid State Chem.* **2022**, *309*, 122951. <https://doi.org/10.1016/j.jssc.2022.122951>.
- 22 Wang, L.; Zhang, F.; Yang, J.; Li, L.; Li, J. The Efficient Separation of N₂O/CO₂ Using Unsaturated Fe²⁺ Sites in MIL-100Fe. *Chem. Commun.* **2021**, *57* (54), 6636–6639. <https://doi.org/10.1039/D1CC01659H>.
- 23 Saha, D.; Bao, Z.; Jia, F.; Deng, S. Adsorption of CO₂, CH₄, N₂O, and N₂ on MOF-5, MOF-177, and Zeolite 5A. *Environ. Sci. Technol.* **2010**, *44* (5), 1820–1826. <https://doi.org/10.1021/es9032309>.
- 24 Wang, L.; Li, Y.; Wang, Y.; Yang, J.; Li, L.; Li, J. Research on CO₂-N₂O Separation Using Flexible Metal Organic Frameworks. *Sep. Purif. Technol.* **2020**, *251*, 117311. <https://doi.org/10.1016/j.seppur.2020.117311>.
- 25 Mercuri, G.; Moroni, M.; Galli, S.; Tuci, G.; Giambastiani, G.; Yan, T.; Liu, D.; Rossin, A. Temperature-Dependent Nitrous Oxide/Carbon Dioxide Preferential Adsorption in a Thiazolium-Functionalized NU-1000 Metal–Organic Framework. *ACS Appl. Mater. Interfaces* **2021**, *13* (49), 58982–58993. <https://doi.org/10.1021/acsami.1c21437>.
- 26 Rieth, A. J.; Tulchinsky, Y.; Dincă, M. High and Reversible Ammonia Uptake in Mesoporous Azolate Metal–Organic Frameworks with Open Mn, Co, and Ni Sites. *J. Am. Chem. Soc.* **2016**, *138* (30), 9401–9404. <https://doi.org/10.1021/jacs.6b05723>.
- 27 Azbell, T. J.; Pitt, T. A.; Bollmeyer, M. M.; Cong, C.; Lancaster, K. M.; Milner, P. J. Ionothermal Synthesis of Metal–Organic Frameworks Using Low-Melting Metal Salt Precursors. *Angew. Chem. Int. Ed.* **2023**, *62* (17), e2022182. <https://doi.org/10.1002/anie.202218252>.
- 28 Park, S. S.; Tulchinsky, Y.; Dincă, M. Single-Ion Li⁺, Na⁺, and Mg²⁺ Solid Electrolytes Supported by a Mesoporous Anionic Cu–Azolate Metal–Organic Framework. *J. Am. Chem. Soc.* **2017**, *139* (38), 13260–13263. <https://doi.org/10.1021/jacs.7b06197>.
- 29 Caskey, S. R.; Wong-Foy, A. G.; Matzger, A. J. Dramatic Tuning of Carbon Dioxide Uptake via Metal Substitution in a Coordination Polymer with Cylindrical Pores. *J. Am. Chem. Soc.* **2008**, *130* (33), 10870–10871. <https://doi.org/10.1021/ja8036096>.
- 30 Bloch, E. D.; Murray, L. J.; Queen, W. L.; Chavan, S.; Maximoff, S. N.; Bigi, J. P.; Krishna, R.; Peterson, V. K.; Grandjean, F.; Long, G. J.; Smit, B.; Bordiga, S.; Brown, C. M.; Long, J. R. Selective Binding of O₂ over N₂ in a Redox-Active Metal–Organic Framework with Open Iron(II) Coordination Sites. *J. Am. Chem. Soc.* **2011**, *133* (37), 14814–14822. <https://doi.org/10.1021/ja205976v>.
- 31 Severin, K. Synthetic Chemistry with Nitrous Oxide. *Chem. Soc. Rev.* **2015**, *44* (17), 6375–6386. <https://doi.org/10.1039/C5CS00339C>.
- 32 Parmon, V. N.; Panov, G. I.; Uriarte, A.; Noskov, A. S. Nitrous Oxide in Oxidation Chemistry and Catalysis: Application and Production. *Catalysis Today* **2005**, *100* (1–2), 115–131. <https://doi.org/10.1016/j.cattod.2004.12.012>.
- 33 Le Vaillant, F.; Mateos Calbet, A.; González-Pelayo, S.; Reijerse, E. J.; Ni, S.; Busch, J.; Cornella, J. Catalytic Synthesis of Phenols with Nitrous Oxide. *Nature* **2022**, *604* (7907), 677–683. <https://doi.org/10.1038/s41586-022-04516-4>.
- 34 Bols, M. L.; Snyder, B. E. R.; Rhoda, H. M.; Cnudde, P.; Fayad, G.; Schoonheydt, R. A.; Van Speybroeck, V.; Solomon, E. I.; Sels, B. F. Coordination and Activation of Nitrous Oxide by Iron Zeolites. *Nat. Catal.* **2021**, *4* (4), 332–340. <https://doi.org/10.1038/s41929-021-00602-4>.
- 35 Simons, M. C.; Prinslow, S. D.; Babucci, M.; Hoffman, A. S.; Hong, J.; Vitillo, J. G.; Bare, S. R.; Gates, B. C.; Lu, C. C.; Gagliardi, L.; Bhan, A. Beyond Radical Rebound: Methane Oxidation to Methanol Catalyzed by Iron Species in Metal–Organic Framework Nodes. *J. Am. Chem. Soc.* **2021**, *143* (31), 12165–12174. <https://doi.org/10.1021/jacs.1c04766>.
- 36 Barona, M.; Ahn, S.; Morris, W.; Hoover, W.; Notestein, J. M.; Farha, O. K.; Snurr, R. Q. Computational Predictions and Experimental Validation of Alkane Oxidative Dehydrogenation by Fe₂M MOF Nodes. *ACS Catal.* **2020**, *10* (2), 1460–1469. <https://doi.org/10.1021/acscatal.9b03932>.
- 37 Xiao, D. J.; Bloch, E. D.; Mason, J. A.; Queen, W. L.; Hudson, M. R.; Planas, N.; Borycz, J.; Dzubak, A. L.; Verma, P.; Lee, K.; Bonino, F.; Crocellà, V.; Yano, J.; Bordiga, S.; Truhlar, D. G.; Gagliardi, L.; Brown, C. M.; Long, J. R. Oxidation of Ethane to Ethanol by N₂O in a Metal–Organic Framework with Coordinatively Unsaturated Iron(II) Sites. *Nat. Chem.* **2014**, *6* (7), 590–595. <https://doi.org/10.1038/nchem.1956>.
- 38 Tofoni, A.; Tavani, F.; Vandone, M.; Braglia, L.; Borfecchia, E.; Ghigna, P.; Stoian, D. C.; Grell, T.; Stolfi, S.; Colombo, V.; D'Angelo, P. Full Spectroscopic Characterization of the Molecular Oxygen-Based Methane to Methanol Conversion over Open Fe(II) Sites in a Metal–Organic Framework. *J. Am. Chem. Soc.* **2023**, *jacs.3c07216*. <https://doi.org/10.1021/jacs.3c07216>.
- 39 Vitillo, J. G.; Choudhary, M.; Simons, M. C.; Gagliardi, L.; Bhan, A. Mechanism of Benzene Hydroxylation on Tri-Iron Oxo-Centered Cluster-Based Metal–Organic Frameworks. *J. Phys. Chem. C* **2023**, *acs.jpcc.3c06423*. <https://doi.org/10.1021/acs.jpcc.3c06423>.
- 40 Verma, P.; Vogiatzis, K. D.; Planas, N.; Borycz, J.; Xiao, D. J.; Long, J. R.; Gagliardi, L.; Truhlar, D. G. Mechanism of Oxidation of Ethane to Ethanol at Iron(IV)–Oxo Sites in Magnesium-Diluted Fe₂(dobdc). *J. Am. Chem. Soc.* **2015**, *137* (17), 5770–5781. <https://doi.org/10.1021/jacs.5b00382>.
- 41 Borycz, J.; Paier, J.; Verma, P.; Darago, L. E.; Xiao, D. J.; Truhlar, D. G.; Long, J. R.; Gagliardi, L. Structural and Electronic Effects on the Properties of Fe₂(dobdc) upon Oxidation with N₂O. *Inorg. Chem.* **2016**, *55* (10), 4924–4934. <https://doi.org/10.1021/acs.inorgchem.6b00467>.
- 42 Suh, B. L.; Kim, J. Ligand Insertion in MOF-74 as Effective Design for Oxidation of Ethane to Ethanol. *J. Phys. Chem. C* **2018**, *122* (40), 23078–23083.
- 43 Costas, M.; Mehn, M. P.; Jensen, M. P.; Que, L. Dioxygen Activation at Mononuclear Nonheme Iron Active Sites: Enzymes, Models, and Intermediates. *Chem. Rev.* **2004**, *104* (2), 939–986. <https://doi.org/10.1021/cr020628n>.
- 44 Wallar, B. J.; Lipscomb, J. D. Dioxygen Activation by Enzymes Containing Binuclear Non-Heme Iron Clusters. *Chem. Rev.* **1996**, *96* (7), 2625–2658. <https://doi.org/10.1021/cr9500489>.
- 45 Meunier, B.; De Visser, S. P.; Shaik, S. Mechanism of Oxidation Reactions Catalyzed by Cytochrome P450 Enzymes. *Chem. Rev.* **2004**, *104* (9), 3947–3980. <https://doi.org/10.1021/cr020443g>.
- 46 Zhuravlev, V.; Malinowski, P. J. A Stable Crystalline Copper(I)–N₂O Complex Stabilized as the Salt of a Weakly Coordinating Anion. *Angew. Chem. Int. Ed.* **2018**, *57* (36), 11697–11700. <https://doi.org/10.1002/anie.201806836>.
- 47 Mokhtarzadeh, C. C.; Chan, C.; Moore, C. E.; Rheingold, A. L.; Figueroa, J. S. Side-On Coordination of Nitrous Oxide to a Mononuclear Cobalt Center. *J. Am. Chem. Soc.* **2019**, *141* (38), 15003–15007. <https://doi.org/10.1021/jacs.9b08241>.

- 48 Piro, N. A.; Lichterman, M. F.; Harman, W. H.; Chang, C. J. A Structurally Characterized Nitrous Oxide Complex of Vanadium. *J. Am. Chem. Soc.* **2011**, *133* (7), 2108–2111. <https://doi.org/10.1021/ja110798w>.
- 49 Pamplin, C. B.; Ma, E. S. F.; Safari, N.; Rettig, S. J.; James, B. R. The Nitrous Oxide Complex $\text{RuCl}_2(\eta^1\text{-N}_2\text{O})(\text{P-N})(\text{PPh}_3)$ (P-N = $[\text{o}-(\text{N,N}\text{-Dimethylamino})\text{phenyl}]\text{diphenylphosphine}$); Low Temperature Conversion of N_2O to N_2 and O_2 . *J. Am. Chem. Soc.* **2001**, *125* (35), 8596–8597. <https://doi.org/10.1021/ja0106319>.
- 50 Paulat, F.; Kuschel, T.; Näther, C.; Praneeth, V. K. K.; Sander, O.; Lehnert, N. Spectroscopic Properties and Electronic Structure of Pentammineruthenium(II) Dinitrogen Oxide and Corresponding Nitrosyl Complexes: Binding Mode of N_2O and Reactivity. *Inorg. Chem.* **2004**, *43* (22), 6979–6994. <https://doi.org/10.1021/ic049302i>.
- 51 Puerta Lombardi, B.; Gendy, C.; Gelfand, B. S.; Bertrand, G. M.; Wasylishen, R. E.; Tuononen, H. M.; Roesler, R. Side-on Coordination in Isostructural Nitrous Oxide and Carbon Dioxide Complexes of Nickel. *Angew. Chem. Int. Ed.* **60** (13), 7077–7081. <https://doi.org/10.1002/anie.202011301>.
- 52 Gyton, M. R.; Leforestier, B.; Chaplin, A. B. Rhodium(I) Pincer Complexes of Nitrous Oxide. *Angewandte Chemie* **2019**, *131* (43), 15439–15442. <https://doi.org/10.1002/ange.201908333>.
- 53 Tolman, W. B. Binding and Activation of N_2O at Transition-Metal Centers: Recent Mechanistic Insights. *Angew. Chem. Int. Ed.* **2010**, *49* (6), 1018–1024. <https://doi.org/10.1002/anie.200905364>.
- 54 Ketrat, S.; Maihom, T.; Wannakao, S.; Probst, M.; Nokbin, S.; Limtrakul, J. Coordinatively Unsaturated Metal–Organic Frameworks $\text{M}_3(\text{btc})_2$ (M = Cr, Fe, Co, Ni, Cu, and Zn) Catalyzing the Oxidation of CO by N_2O : Insight from DFT Calculations. *Inorg. Chem.* **2017**, *56* (22), 14005–14012. <https://doi.org/10.1021/acs.inorgchem.7b02143>.
- 55 Rieth, A. J.; Wright, A. M.; Skorupskii, G.; Mancuso, J. L.; Hendon, C. H.; Dincă, M. Record-Setting Sorbents for Reversible Water Uptake by Systematic Anion Exchanges in Metal–Organic Frameworks. *J. Am. Chem. Soc.* **2019**, *141* (35), 13858–13866. <https://doi.org/10.1021/jacs.9b06246>.
- 56 Zick, M. E.; Lee, J.-H.; Gonzalez, M. I.; Velasquez, E. O.; Uliana, A. A.; Kim, J.; Long, J. R.; Milner, P. J. Fluoroarene Separations in Metal–Organic Frameworks with Two Proximal Mg^{2+} Coordination Sites. *J. Am. Chem. Soc.* **2021**, *143* (4), 1948–1958. <https://doi.org/10.1021/jacs.0c11530>.
- 57 Geier, S. J.; Mason, J. A.; Bloch, E. D.; Queen, W. L.; Hudson, M. R.; Brown, C. M.; Long, J. R. Selective Adsorption of Ethylene over Ethane and Propylene over Propane in the Metal–Organic Frameworks $\text{M}_2(\text{dobdc})$ (M = Mg, Mn, Fe, Co, Ni, Zn). *Chem. Sci.* **2013**, *4* (5), 2054–2061. <https://doi.org/10.1039/c3sc00032j>.
- 58 Gonzalez, M. I.; Kapelewski, M. T.; Bloch, E. D.; Milner, P. J.; Reed, D. A.; Hudson, M. R.; Mason, J. A.; Barin, G.; Brown, C. M.; Long, J. R. Separation of Xylene Isomers through Multiple Metal Site Interactions in Metal–Organic Frameworks. *J. Am. Chem. Soc.* **2018**, *140* (9), 3412–3422. <https://doi.org/10.1021/jacs.7b13825>.
- 59 Mason, J. A.; Veenstra, M.; Long, J. R. Evaluating Metal–Organic Frameworks for Natural Gas Storage. *Chem. Sci.* **2014**, *5* (1), 32–51. <https://doi.org/10.1039/C3SC52633J>.
- 60 Sumida, K.; Stück, D.; Mino, L.; Chai, J.-D.; Bloch, E. D.; Zavorotynska, O.; Murray, L. J.; Dincă, M.; Chavan, S.; Bordiga, S.; Head-Gordon, M.; Long, J. R. Impact of Metal and Anion Substitutions on the Hydrogen Storage Properties of M-BTT Metal–Organic Frameworks. *J. Am. Chem. Soc.* **2013**, *135* (3), 1083–1091. <https://doi.org/10.1021/ja310173e>.
- 61 Irving, H.; Williams, R. J. P. Order of Stability of Metal Complexes. *Nature* **1948**, *162*, 746–747. <https://doi.org/10.1038/162746a0>.
- 62 Yu, D.; Yazaydin, A. O.; Lane, J. R.; Dietzel, P. D. C.; Snurr, R. Q. A Combined Experimental and Quantum Chemical Study of CO_2 Adsorption in the Metal–Organic Framework CPO-27 with Different Metals. *Chem. Sci.* **2013**, *4* (9), 3544–3556. <https://doi.org/10.1039/c3sc51319j>.
- 63 Rosnes, M. H.; Sheptyakov, D.; Franz, A.; Frontzek, M.; Dietzel, P. D. C.; Georgiev, P. A. On the Elusive Nature of Oxygen Binding at Coordinatively Unsaturated 3d Transition Metal Centers in Metal–Organic Frameworks. *Phys. Chem. Chem. Phys.* **2017**, *19* (38), 26346–26357. <https://doi.org/10.1039/C7CP05119K>.
- 64 Barona, M.; Snurr, R. Q. Exploring the Tunability of Trimetallic MOF Nodes for Partial Oxidation of Methane to Methanol. *ACS Appl. Mater. Interfaces* **2020**, *12* (25), 28217–28231. <https://doi.org/10.1021/acsami.0c06241>.
- 65 Zhang, Q.; Li, B.; Chen, L. First-Principles Study of Microporous Magnets M-MOF-74 (M = Ni, Co, Fe, Mn): The Role of Metal Centers. *Inorg. Chem.* **2013**, *52* (16), 9356–9362. <https://doi.org/10.1021/ic400927m>.
- 66 Bloch, E. D.; Queen, W. L.; Krishna, R.; Zadrozny, J. M.; Brown, C. M.; Long, J. R. Hydrocarbon Separations in a Metal–Organic Framework with Open Iron(II) Coordination Sites. *Science* **2012**, *335* (6076), 1606–1610. <https://doi.org/10.1126/science.1217544>.
- 67 Vogiatzis, K. D.; Haldoupis, E.; Xiao, D. J.; Long, J. R.; Siepmann, J. I.; Gagliardi, L. Accelerated Computational Analysis of Metal–Organic Frameworks for Oxidation Catalysis. *J. Phys. Chem. C* **2016**, *120* (33), 18707–18712. <https://doi.org/10.1021/acs.jpcc.6b07115>.
- 68 Vitillo, J. G.; Lu, C. C.; Cramer, C. J.; Bhan, A.; Gagliardi, L. Influence of First and Second Coordination Environment on Structural Fe(II) Sites in MIL-101 for C–H Bond Activation in Methane. *ACS Catal.* **2021**, *11* (2), 579–589. <https://doi.org/10.1021/acscatal.0c03906>.
- 69 Larson, V. A.; Battistella, B.; Ray, K.; Lehnert, N.; Nam, W. Iron and Manganese Oxo Complexes, Oxo Wall and Beyond. *Nat. Rev. Chem.* **2020**, *4* (8), 404–419. <https://doi.org/10.1038/s41570-020-0197-9>.
- 70 Yamashita, T.; Vannice, A. N_2O Decomposition over Manganese Oxides. *Journal of Catalysis* **1996**, *161* (1), 254–262. <https://doi.org/10.1006/jcat.1996.0183>.
- 71 Ross, R. A.; Fairbridge, C. Oxidation of 1-Butene by Nitrous Oxide over Manganese(III) and Related Transition Metal Oxides. *Can. J. Chem.* **1984**, *62* (8), 1483–1486. <https://doi.org/10.1139/v84-252>.
- 72 Ben-Daniel, R.; Weiner, L.; Neumann, R. Activation of Nitrous Oxide and Selective Epoxidation of Alkenes Catalyzed by the Manganese-Substituted Polyoxometalate, $[\text{Mn}^{\text{III}}_2\text{ZnW}(\text{Zn}_2\text{W}_9\text{O}_{34})_2]^{10-}$. *J. Am. Chem. Soc.* **2002**, *124* (30), 8788–8789. <https://doi.org/10.1021/ja0259077>.
- 73 Jiang, M.-X.; Liu, C.-G. New Insight into the Catalytic Cycle about Epoxidation of Alkenes by N_2O over a Mn-Substituted Keggin-Type Polyoxometalate. *Journal of Molecular Graphics and Modelling* **2017**, *73*, 8–17. <https://doi.org/10.1016/j.jmgm.2016.12.012>.
- 74 Li, Y.; Armor, J. N. Catalytic Decomposition of Nitrous Oxide on Metal Exchanged Zeolites. *Appl. Catal. B* **1992**, *1* (3), L21–L29. [https://doi.org/10.1016/0926-3373\(92\)80019-V](https://doi.org/10.1016/0926-3373(92)80019-V).
- 75 Campa, M. C.; Indovina, V.; Pietrogiacomi, D. The Selective Catalytic Reduction of N_2O with CH_4 on Na-MOR and Na-MFI Exchanged with Copper, Cobalt or Manganese. *Applied Catalysis B: Environmental* **2012**, *111–112*, 90–95. <https://doi.org/10.1016/j.apcatb.2011.09.021>.
- 76 Cozzolino, A. F.; Brozek, C. K.; Palmer, R. D.; Yano, J.; Li, M.; Dincă, M. Ligand Redox Non-Innocence in the Stoichiometric

- Oxidation of Mn₂(2,5-dioxidoterephthalate) (Mn-MOF-74). *J. Am. Chem. Soc.* **2014**, *136* (9), 3334–3337. <https://doi.org/10.1021/ja411808r>.
- 77 Halbach, R. L.; Gygi, D.; Bloch, E. D.; Anderson, B. L.; Nocera, D. G. Structurally Characterized Terminal Manganese(IV) Oxo Tris(Alkoxide) Complex. *Chem. Sci.* **2018**, *9* (19), 4524–4528. <https://doi.org/10.1039/C8SC01164H>.
- 78 Wang, X.; Andrews, L. Infrared Spectra of M(OH)_{1,2,3} (M = Mn, Fe, Co, Ni) Molecules in Solid Argon and the Character of First Row Transition Metal Hydroxide Bonding. *J. Phys. Chem. A* **2006**, *110* (33), 10035–10045. <https://doi.org/10.1021/jp0624698>.
- 79 Canivet, J.; Fateeva, A.; Guo, Y.; Coasne, B.; Farrusseng, D. Water Adsorption in MOFs: Fundamentals and Applications. *Chem. Soc. Rev.* **2014**, *43* (16), 5594–5617. <https://doi.org/10.1039/C4CS00078A>.